# Investigation into the mercury intrusion porosimetry (MIP) and micro-computed tomography ($\mu$CT) methods for determining the pore size distribution of MX80 bentonite pellet

Jin-Wen Yang, Yu-Jun Cui, Nadia Mokni, Emmanuel Ormea

## To cite this version:

Jin-Wen Yang, Yu-Jun Cui, Nadia Mokni, Emmanuel Ormea. Investigation into the mercury intrusion porosimetry (MIP) and micro-computed tomography ($\mu$CT) methods for determining the pore size distribution of MX80 bentonite pellet. Acta Geotechnica, 2024, 19, pp.85-97. 10.1007/s11440-023-01863-y . irsn-04311821

HAL Id: irsn-04311821
https://irsn.hal.science/irsn-04311821
Submitted on 7 Dec 2023

# Investigation into the Mercury Intrusion Porosimetry (MIP) and Micro-Computed Tomography (μCT) methods for determining the pore size distribution of MX80 bentonite pellet

Jin-Wen Yang[1*], Yu-Jun Cui[1], Nadia Mokni[2], Emmanuel Ormea[3]

[1]Ecole des Ponts ParisTech, Laboratoire Navier/CERMES, 6 et 8 avenue Blaise Pascal, 77455 Marne La Vallée cedex 2, France

[2]Institut de Radioprotection et de Sûreté Nucléaire (IRSN), Fontenay-aux-Roses, France

[3]Aergon, 8 rue Édouard Naud, 92130 Issy-les-Moulineaux, France

***Corresponding author:**
Mr. Jin-Wen Yang
Ecole des Ponts ParisTech
6-8 av. Blaise Pascal, Cité Descartes, Champs-sur-Marne
77455 Marne-la-Vallée cedex 2
France
E-mail : jinwen.yang@enpc.fr

## Abstract

The pore size distribution (PSD) plays an important role in the hydro-mechanical behaviour for porous materials. In this study, the PSD of MX80 bentonite pellets under various imposed suctions from 262 to 1.5 MPa was determined by both Mercury Intrusion Porosimetry (MIP) and Micro-Computed Tomography (μCT). The void ratios $e_{18\text{-}344}$ in the overlapping pore range (18-344 μm) identified by MIP and μCT were compared to clarify the difference between the two techniques. Results showed that the MIP-detection $e_{18\text{-}344}$ nearly overlapped with the μCT-detection one at suction $s \geq 57$ MPa, indicating the reliability of MIP and μCT results for pellets at $s \geq 57$ MPa. However, the μCT-detection $e_{18\text{-}344}$ became larger than the MIP-detection one at 9 MPa $\leq s \leq$ 38 MPa, while the changes of MIP-detection and μCT-detection $e_{18\text{-}344}$ with suctions were opposite at $s \leq 4.2$ MPa. As the difficulty of interpreting the variation of μCT attenuation coefficient at low suctions undermined the reliability of μCT thresholding, the segmentation of μCT images was suggested to be determined by making the μCT-detection $e_{18\text{-}344}$ equal to the MIP-detection one. Because the reliability of MIP results at $s \leq 4.2$ MPa was reduced by the difficulty of keeping the integrity of freeze-dried samples, the MIP-detection $e_{18\text{-}344}$ determined in a previous study without the sample integrity problem was chosen as reference for the μCT thresholding at 1.5 MPa $\leq s \leq$ 4.2 MPa. The corrected μCT-detection $e_{18\text{-}344}$ calculated by the new thresholds matched well with the MIP-detection $e_{18\text{-}344}$, completing the μCT-detection at suctions smaller than 57 MPa. Since the MIP-detection PSD only covers the pores smaller than 344 μm, the μCT-detection PSD with pores larger than 344 μm was then integrated into the MIP-detection PSD, enlarging the MIP-detection to millimetric pores.

**Keywords**: bentonite pellet; suction; Mercury Intrusion Porosimetry; Micro-Computed Tomography; pore size distribution.

## 1. Introduction

In the European concepts of deep geological disposal for high-level waste, a multi-barrier system consisting of metal canisters, natural geological barrier (host rock), concrete lining and sealing/backfill elements (bentonite-based materials) has been adopted [11, 37]. To well understand the hydro-mechanical behaviour of the involved porous materials (host rock, bentonite-based materials and concrete), it is important to identify their pore size distributions (PSDs) [2, 5, 14, 37]. Indeed, the PSDs can help reveal the microstructure [19, 23, 33], determine the damage coefficient by extracting the macro-porosity [18, 30].

Mercury Intrusion Porosimetry (MIP) that is based on the measurement of the volume of mercury intruded into pores with distinct sizes under different intrusion pressures, is a widely-applied technique in detecting the PSDs of porous media, due to its advantages including high efficiency, great accuracy and a broad pore-detection range (from several nano-meters to several hundreds of micro-meters) [23, 30]. However, the MIP technique is unable to detect pores with sizes larger than several hundreds of micro-meters and smaller than several nano-meters. By contrast, Micro-Computed Tomography (μCT) is a non-destructive technique that can visually reveal the pore structure of porous materials in high resolution (tens of micrometers) without particular sample preparation [13]. The μCT can detect pores larger than the μCT resolution, but the difficulty and uncertainty in image segmentation is a major concern [3, 13] because a tiny adjustment of grey threshold can significantly affect the final result. Hence, it is important to study the PSD with both MIP and μCT techniques in order to extend the detection pore range from several nano-meters to several millimeters.

A few studies were performed on the PSD of porous materials with MIP and μCT techniques [17, 39]. Zong et al. [39] conducted Nitrogen Adsorption/desorption Isotherms (NAIs), MIP tests and Synchrotron-Radiation-based X-ray computed microtomography (SR-μCT) on four types of soils, including black soils, Shajiang black soil, paddy soil and latosolic red soil. They observed that for the overlapping pore region with the three methods, the PSDs detected by the MIP and SR-μCT methods agreed well for the pores larger than 3.75 μm and smaller than 360 μm, while NAIs highly underestimated the PSD compared with MIP for the pores larger than 0.003 μm and smaller than 0.15 μm. Li and Shao [17] performed one MIP test and two μCT scans with two resolutions (10 μm and 40 μm) on loess. The equivalent sphere diameter was employed for the comparison of MIP and μCT results in their common range. It was observed that the MIP-detection void ratio was larger than the two μCT-detection ones for the pores larger than 15.6 μm and smaller than 200 μm, whereas the MIP-detection void ratio became smaller than the two μCT-detection ones for the pores larger than 200 μm and smaller than 400 μm. Additionally, the μCT-detection void ratio with resolution of 10 μm was closer to the MIP-detection void ratio compared with resolution of 40 μm, showing that the lower the μCT resolution, the smaller the difference between MIP and μCT results.

Some studies did not aim at PSD investigation, but compared MIP and μCT from a perspective of visualizing mercury by μCT after MIP tests [34–36]. Zeng et al. [36] and Zeng et al. [35] conducted μCT scan on post-MIP porous cement and the μCT results revealed that most detected pores were entrapped by mercury with a few unfilled pores (possibly resulting from the ink-bottle effect after mercury extrusion [35], showing a good agreement between MIP and μCT. The study with μCT scanning on post-MIP compacted clay also showed that the μCT can well identify the mercury entrapped by the ink-bottle effect [34]. Zeng et al. [36] and Zeng et al. [35] pointed out that nearly all mercury-entrapped pores within porous cement were spherically-shaped due to the naturally hydrophobic feature of mercury. Moreover, the smaller the pore diameter, the larger the sphericity of pores. However, Yuan et al. [34] reported that the most mercury-entrapped pores within clay are non-spherically-shaped, suggesting that the mercury intrusion or extrusion would not misrepresent the pore structure. Hence, from the aforementioned studies, it appears that there is generally a good agreement between μCT and MIP in their overlapping pore range. However, to the authors' knowledge, no studies tried to make an extension of the detection pore range using both the MIP and μCT techniques, in particular for soils at different suctions.

In this study, the μCT and MIP techniques were employed to determine the PSD of bentonite pellets under different suctions from 262 to 1.5 MPa. The void ratio of the pores with overlapping pore range from 18 to 344 μm ($e_{18\text{-}344}$) were analysed to compare the two techniques. A method for extending the PSDs was finally proposed.

## 2. Materials and Methods

The investigated material is MX80 bentonite pellet. This bentonite in powder form comes from Wyoming, USA, containing a high smectite content (80%) and some other non-clay minerals (8% anorthite, 4% quartz, 4% muscovite, 2% albite and < 1% pyrite) [20]. Bentonite powder was rapidly and powerfully compacted into a mould of approximately 32 mm in diameter and 32 mm in height to fabricate the pellets (Fig. 1(a)) which have a commercial name of Expangel SP32 [20]. The top and bottom semi-spherical caps were excised using a cutting machine and smoothened using sandpapers to produce cylinder-shaped pellets (Fig. 1(b)) in order to ensure an easier measurement of volume and a better definition of stress state. The initial hydro-mechanical properties of pellets are presented in Table 1. The treated pellets were carefully placed in desiccators with desired saturated salt solutions at constant 20 ℃ temperature for imposing suctions from 262 to 4.2 MPa. According to Tang and Cui [28], various salt solutions were chosen, including LiCl for 262 MPa, $MgCl_2$ for 149 MPa, $K_2CO_3$ for 113 MPa, $Mg(NO_3)_2$ for 82 MPa, NaCl for 38 MPa, $(NH_4)_2SO_4$ for 25 MPa, $KNO_3$ for 9 MPa and $K_2SO_4$ for 4.2 MPa. Some pellets were also placed inside a plastic box with deionized water on the bottom for the target suctions smaller than 4.2 MPa. After two months, a filter paper was pasted onto the top cover and deionized water was evenly sprayed on the filter paper every two days to accelerate the wetting process with target suctions. The pellets were regularly taken out to measure the mass, height and diameter for determining the water content $w$ and the total void ratio $e_T$. In order to avoid the damage on pellets at $s \leq 4.2$ MPa, only the mass was measured and thus only the water content was determined for these pellets.

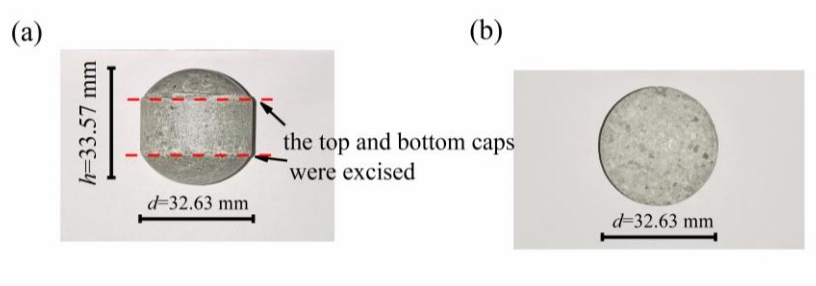

Fig. 1. MX80 bentonite pellets: (a) original pellet; (b) machined pellet.

Table. 1. Initial hydro-mechanical properties of pellets

| Property | Value |
|---|---|
| Dry density, $\rho_d$: Mg/m$^3$ | 2.08 |
| Void ratio, $e$ | 0.37 |
| Water content, $w$ % | 6.32 |
| Diameter, $D$: mm | 32.63 |
| Height, $H$: mm | 11.51 |
| Suction, $s$: MPa | 114.36 |

The variations of water content $w$ and total void ratio $e_T$ with time are presented in Fig. 2. The absence of data from the 30th to 100th day was due to the lockdown of France in March and April 2020. It is observed that the pellets at $s \leq 82$ MPa swelled with absorption of water and the pellets at $s \geq 149$ MPa shrank with loss of water, suggesting that the initial suction of pellets was between 82 and 149 MPa. All the pellets finally reached the target suctions.

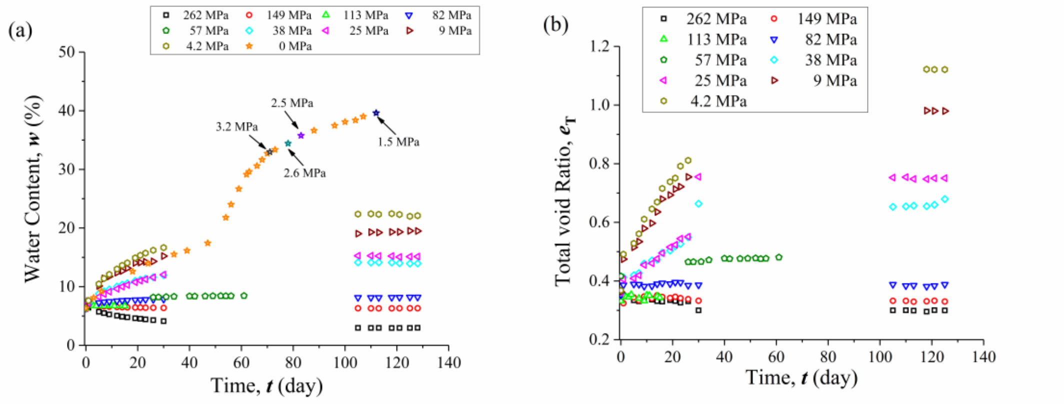

Fig. 2. (a) Water content $w$ versus time; (b) Total void ratio $e_T$ versus time.

After the pellets reached the target suctions, several centimetric samples were cut out from the centre and the perimeter of pellets, which were then freeze-dried according to the procedure proposed by Delage et al. [6]. A Micromeritics Auto-pore IV 9500 mercury intrusion porosimeter was used to explore the porous structure of samples under a working pressure from 3.4 kPa to 227.5 MPa, allowing identification of the entrance diameters from 344 μm to 5.5 nm. Some other pellets were waxed to avoid water loss by evaporation for future μCT scans by Skyscanner-1173. The voltage and current of X-ray sources are 130 kV and 61 μA, respectively, with a 0.25mm-thick copper filter placed in front of the sources. These settings allowed reducing the noise and increasing the image quality and contrast [8, 16, 29]. The whole pellet was scanned using 2240×2240 pixels into 16-bit BMP-format images with voxel size of 18 μm. After scans, the bentonite pellet was 3D reconstructed by assembling around 700 horizontal slices using Bruker software NRecon with median noise reduction.

## 3. Calibration of MIP-Detection and μCT-Detection $e_{18\text{-}344}$

The MIP and μCT techniques have distinct detection ranges of pores as presented in Fig. 3. Within a particle, the smectite layers are disposed one above another in a face-to-face orientation, with the planar interlayer space between the elementary smectite layers, inside the smectite particles. The smectite particles are assembled together inside the aggregates with inter-particle pores. Between aggregates there are large inter-aggregate pores [6]. The intra-aggregate pores comprise the interlayer space and the inter-particle pores. The interlayer space and the inter-particle pores smaller than 5.5 nm and the inter-aggregate pores larger than 344 μm are undetectable by the MIP technique. By contrast, the μCT can only detect the inter-aggregate pores larger than 18 μm (the μCT-detection pores). Therefore, the μCT-recognized bentonite fabric includes the bentonite matrix and the μCT-non-detection pores (intra-aggregate pores and inter-aggregate pores smaller than 18 μm). The pores between 18 and 344 μm (with the void ratio $e_{18\text{-}344}$) are the overlapping pore size range that both the MIP and μCT can detect. Thus, the MIP-detection and μCT-detection $e_{18\text{-}344}$ are compared and analysed in this study.

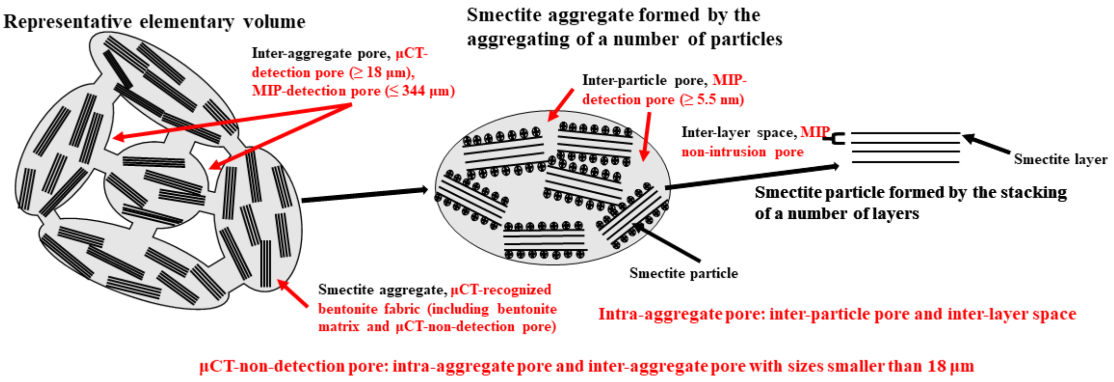

Fig. 3. Classificatrion of pores detectable by both MIP and μCT.

### 3.1 Calibration of MIP-detection $e_{18\text{-}344}$

In MIP tests, the Washburn equation was used in calculating the corresponding pore entrance diameter $D$ (μm) [32]:

$$D = \frac{4T_S \cos\alpha}{P} \qquad (1)$$

where $P$ (MPa) is the mercury pressure, $T_s$ is the interfacial tension (taken equal to 0.485 N/m), $\alpha$ is the contact angle between the mercury-air interface and soil (taken equal to 130° as in plenty of literatures for bentonite [12, 27, 30, 38]).

In MIP tests, 10 seconds were adopted for pressure lower than 0.21 MPa and 120 seconds were adopted for pressure larger than 0.21 MPa between each pressure step. It is worth noting that sufficient time must be let to allow the quasi-static condition to be reached, so that a constant contact angle could be adopted [1, 23].

Fig. 4 shows the cumulative void ratio versus the entrance pore diameter for the bentonite pellets at suctions 82 and 4.2 MPa. The MIP-detection $e_{18\text{-}344}$ was extracted from the cumulative curves.

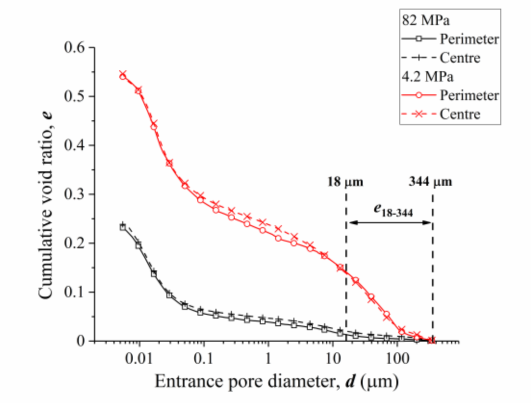

Fig. 4. MIP-detection cumulative void ratios of pellets at suctions 82 and 4.2 MPa.

### 3.2 Calibration of μCT-detection $e_{18\text{-}344}$

The μCT-scanned specimen usually consists of several discrete phases with distinct phase contrasts (in this study, one phase was bentonite fabric and another μCT-detection pores). The segmentation of bentonite fabric and μCT-detection pores is of great interest for the computational purpose - the determination of the grey level threshold. The thresholding process is thus essential in image analysis. The automatic thresholding and the manual thresholding are two methods commonly used in determining the grey level threshold. The automatic thresholding is based on either the histogram of pixel density distribution along grey level such as the OTSU method [22, 25], the Valley-emphasis method [9], or the distribution and contrast of pixels within images such as the Watershed method [21] and the Neural network [4]. A minor change in automatic thresholding results in largely different characterisation of microstructure. The manual thresholding directly analyses the μCT images by distinguishing different scanned phases through their distinct grey levels in pixels. Thus, it can be used in assisting the determination of grey level threshold. In this study, the Stanford segmentation that applies the automatic thresholding and the manual thresholding [3] was used.

The automatic thresholding that employed the OTSU method [22, 25] and the Valley-emphasis method [9] worked on the histogram of pixel density distribution along grey level (Fig. 5), but failed when this histogram was unimodal or close to unimodal for suctions 262-38 MPa. The 2nd and 3rd columns of Table 2 show the grey level thresholds calculated from OTSU and Valley-emphasis methods. The manual thresholding is presented in Fig. 6 for suctions 82 and 4.2 MPa as examples. For suction 82 MPa, the automatic thresholding recommended the value 100 as the threshold, but the manual thresholding shows that some minerals were mistakenly treated as pores when choosing threshold greater than 70. As a result, the porosity of pellet was irrationally overestimated. It appears that the binarized pictures at threshold 60 can represent the characteristics of pores. Therefore, 60 was taken as the threshold at $s$ = 82 MPa. As for $s$ = 4.2 MPa, the automatic thresholding suggested the value between 45.9832 and 35.1569. However, the manual thresholding in Fig. 6 shows that the binarized pictures with threshold ≤ 40 failed to depict the profile and shape of the cracks inside the red dotted-line ellipse in the original pictures. Additionally, the grey levels of representative pixels from a small rectangle are presented in the zoom-in figure, with different colours of pixels for grey level below and above 45 (more black and more grey, respectively). Therefore, the value of 45 was chosen as the threshold at suction 4.2 MPa. The thresholds determined are presented in the fourth column of Table 2.

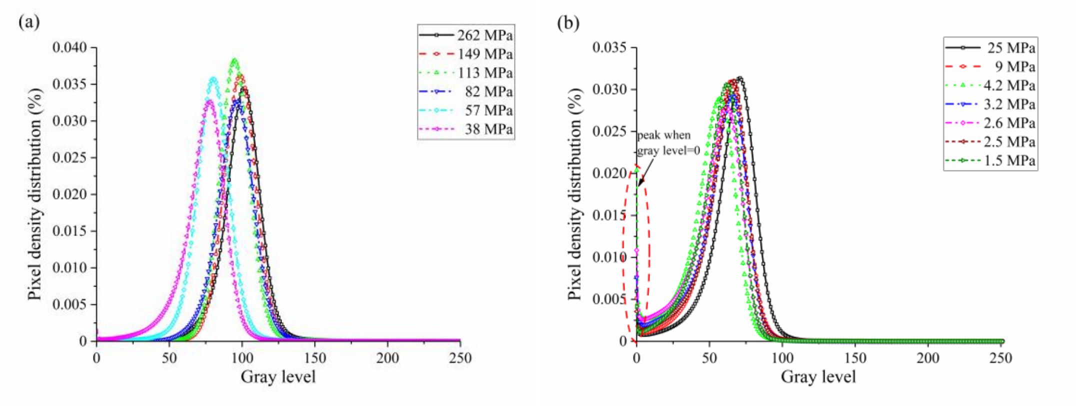

Fig. 5. Pixel density distribution with gray level.

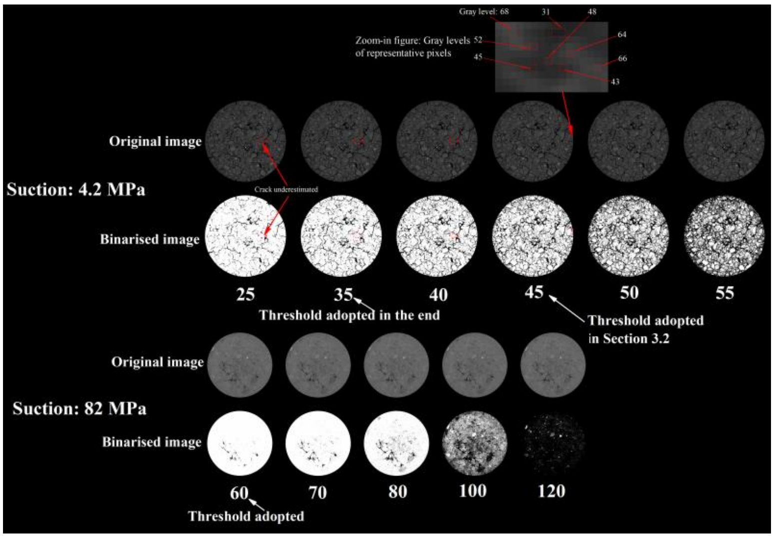

Fig. 6. Manual thresholding at suctions 82 and 4.2 MPa.

Table 2. Summary of grey level thresholds.

| Suction (MPa) | OTSU | Valley-emphasis | Thresholds adopted |
|---|---|---|---|
| 262 | 102.1783 | 139.8733 | 70 |
| 149 | 102.7892 | 141.4752 | 70 |
| 113 | 103.2123 | 123.3823 | 65 |
| 82 | 102.7974 | 123.8752 | 60 |
| 57 | 79.5246 | 97.7145 | 50 |
| 38 | 69.3227 | 54.1365 | 50 |
| 25 | 59.5523 | 45.5459 | 50 |
| 9 | 54.3526 | 42.1858 | 50 |
| 4.2 | 45.9832 | 35.1569 | 45 |
| 3.2 | 47.9171 | 41.2372 | 45 |

| | | | |
|---|---|---|---|
| 2.6 | 46.6723 | 40.5973 | 45 |
| 2.5 | 50.5592 | 44.1436 | 45 |
| 1.5 | 47.3634 | 39.4350 | 45 |

The attenuation coefficient is a measure of how easily a material can be penetrated by an incident energy beam of X-rays. Table 3 shows the average attenuation coefficients and densities of different phases, with the larger attenuation coefficient for higher density. Fig. 7(a) shows that the average attenuation coefficient of sample decreased with suction decreasing from 262 to 4.2 MPa and then increased with further suction decrease. According to Van Geet et al. [10], the larger the average attenuation coefficient of the whole sample, the larger the μCT-recognition density, the smaller the μCT-detection void ratio $e_{\geq 18}$. Therefore, the variation trends of the average attenuation coefficient of whole sample and $e_{\geq 18}$ should be opposite with suction decrease, as shown in Fig. 7(a) for the average attenuation coefficient and in Fig. 7(b) for $e_{\geq 18}$. Additionally, the average attenuation coefficients with similar magnitudes corresponded to the same or similar thresholds.

Table 3. Average attenuation coefficient of different phases in μCT scan.

| Phase | Attenuation coefficient | Density (g/cm$^3$) |
|---|---|---|
| Aluminium | 0.00991 | 2.7 |
| Glass | 0.00972 | 2.5 |
| Free water | 0.00278 | 1.0 |
| Wax | 0.00194 | 0.9 |
| Air | 0.001 | 0.001205 |

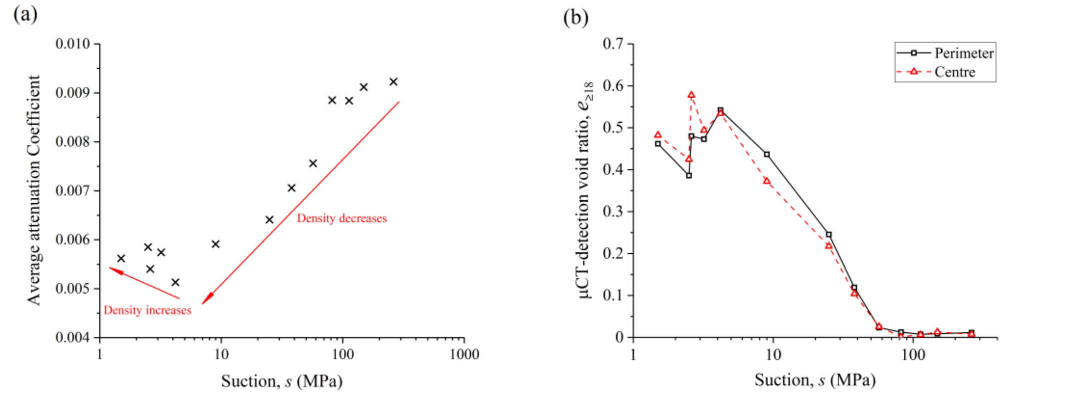

Fig. 7. (a) Average attenuation coefficient of whole sample versus suction; (b) μCT-detection void ratio $e_{\geq 18}$ versus suction.

The μCT images were then transformed into binarized images with only black and white colours, by replacing the pixels below and above the threshold adopted with 0 (black) and 255 (white), respectively. Note that black represents crack and white bentonite fabric. The void ratio of each pore range $i$ with sizes $18i$-$18(i+1)$ μm was calculated by Eq. (2):

$$\mathrm{d}e_{\mathrm{i}} = \frac{\mathrm{d}V_{\mathrm{pore,i}}}{\frac{m}{(1+w)}} G_{\mathrm{S}} \qquad (2)$$

where $V_{\mathrm{pore,i}}$ is the volume of $i^{\mathrm{th}}$ pore range, $m$ the mass, $w$ the water content and $G_{\mathrm{s}}$ the specific gravity (taken as 2.77).

The variation of cumulative void ratio with entrance pore diameter was calculated using Eq. (2) and presented in Fig. 8. The μCT-detection $e_{18\text{-}344}$ was extracted from the cumulative curves.

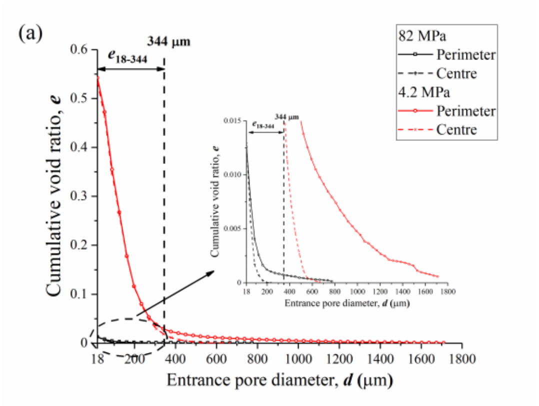

Fig. 8. μCT-detection cumulative void ratios of pellets at suctions 82 and 4.2 MPa.

## 4. Comparison and Discussions

### 4.1 Comparison between MIP-detection and μCT-detection $e_{18\text{-}344}$

The pores between 18 and 344 μm are the overlapping pore size range that both the MIP and μCT can detect, with their void ratios $e_{18\text{-}344}$ compared and analysed in this study. Note that the initial dry densities, void ratios and water contents of 7mm-in-size MX80 bentonite pellet of Molinero-Guerra et al. [19] and 32-mm pellet in this study were close to each other. The fabrications of these two pellets were the same, by heavily compacting powder grains in the mould of different sizes. Fig. 9 depicts the variations of MIP-detection and μCT-detection $e_{18\text{-}344}$ with suctions, together with the results of Molinero-Guerra et al. [19] on 7-mm pellet. The difference between MIP-detection and μCT-detection $e_{18\text{-}344}$ appears negligible at $s \geq 57$ MPa, whereas the μCT-detection $e_{18\text{-}344}$ was remarkably larger than the MIP-detection one at 4.2 MPa $\leq s \leq$ 38 MPa. Both MIP-detection and μCT-detection $e_{18\text{-}344}$ show a large scatter at 1.5 MPa $\leq s \leq$ 4.2 MPa. The trend lines were drawn and it appears that the μCT-detection $e_{18\text{-}344}$ decreased with suction decreasing, unlike the MIP-detection $e_{18\text{-}344}$ which exhibited a remarkable increase in this suction range. The difference between the MIP-detection $e_{18\text{-}344}$ of this study and Molinero-Guerra et al. [19] remained limited at $s \geq 9$ MPa, but large at $s \leq 4.2$ MPa.

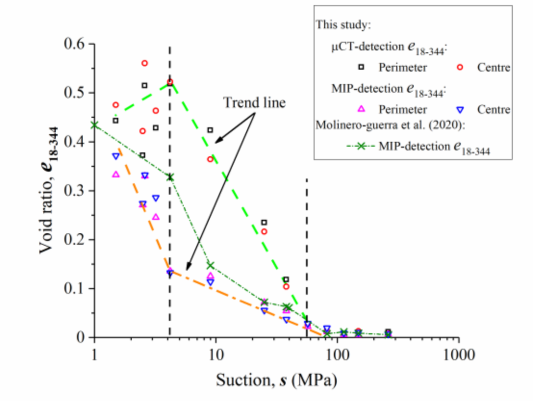

Fig. 9. $e_{18\text{-}344}$ versus suction.

### 4.2 Discussions on MIP results

Although the MIP technique is a widely-recognized technique in determining pore size distribution, it presents some limitations [23, 30]: (1) closed pores: pores are completely surrounded by the aggregated solid particles and isolated from any surrounding mercury-filled pores, even though such closed pores are not significant in soils [23]; (2) constricted pores: large pores that are accessible only through smaller ones, cannot be detected until the smaller pores are penetrated, leading to an underestimation of diameter of some large pores.

The 3D reconstruction of bentonite pellet and pore network at suctions 262, 82 and 9 MPa are presented in Fig. 10, allowing the problems of the closed pores and constricted pores to be analysed. As for high suctions (262 and 82 MPa), it is observed that the pores with sizes ≥ 200 μm were mainly located at the boundary part of pellet and the pores with sizes ≥ 18 μm appeared to extend from boundary to centre and to clump together. Therefore, mercury can always enter the bentonite pellet from the larger pores into the smaller ones. The effects of closed pores and constricted pores were thus quite limited on the PSDs of pellets at high suctions. For pellet at $s$ = 9 MPa, both pores with sizes ≥ 200 μm and pores with sizes ≥ 18 μm appear to be omnipresent within pellets and highly interconnected, indicating that the problem of closed pores and constricted pores can be ignored for the bentonite pellets at low suctions.

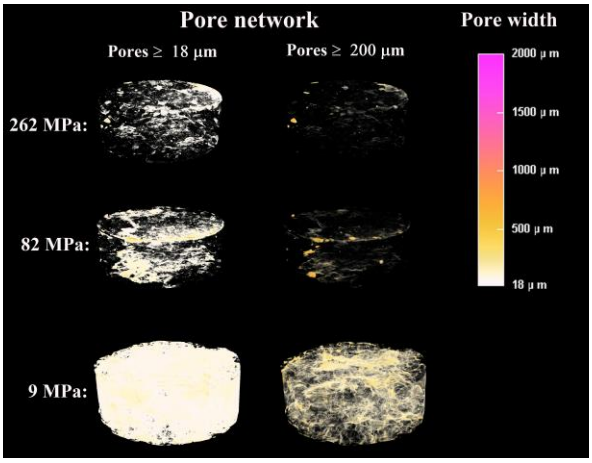

Fig. 10. 3D reconstruction of bentonite pellet and pore network at suctions 262, 82 and 9 MPa.

The exfoliation of particles is significant for bentonite materials at low suctions [6, 31]. The average number of layers per clay particle may decrease from 350 to 10 layers as the suction decreases from 100 to 2 MPa [24]. This leads to increasingly spatially-separated disruption, dispersion of smectite layers and exfoliated particles. Under the electrostatic effect, the microstructure of whole bentonite pellet appears to be of a honeycomb type [7]. The large data scatter at $s \leq 4.2$ MPa observed in Fig. 11(a) resulted from the hydration under a very low suction, which made the sample shape difficult to be kept as shown in Fig. 11(a). This large data scatter led to a large discreteness between MIP-detection and μCT-detection $e_{18\text{-}344}$ at 1.5 MPa $\leq s \leq$ 4.2 MPa in Fig. 9.

The observed difference in MIP-detection $e_{18\text{-}344}$ between this study and Molinero-Guerra et al. [19] at $s \leq 4.2$ MPa might come from the sampling procedure. Molinero-Guerra et al. [19] directly freeze-dried and conducted MIP tests with three 7mm-in-size bentonite pellets in the penetrometer tube, avoiding the disturbance of MIP samples. On the contrary, in this study, one centimetric freeze-dried sample at $s \geq 9$ MPa or two or three millimetric freeze-dried samples at $s \leq 4.2$ MPa were taken out from the 32mm-in-size bentonite pellet because such 32mm-in-size pellet was too large for the penetrometer tube employed (Fig. 11(b)). In fact, the relatively fragmentary millimetric freeze-dried sample at $s \leq 4.2$ MPa was apt to be taken out from a pellet along large crack, causing some underestimation of pore volume. Summarising, the MIP technique is appropriate for identifying the PSD of bentonite pellets. However, the difficulty of keeping good sample shape and the possible effect of sampling should be taken into account while analysing the results for suctions lower than 4.2 MPa.

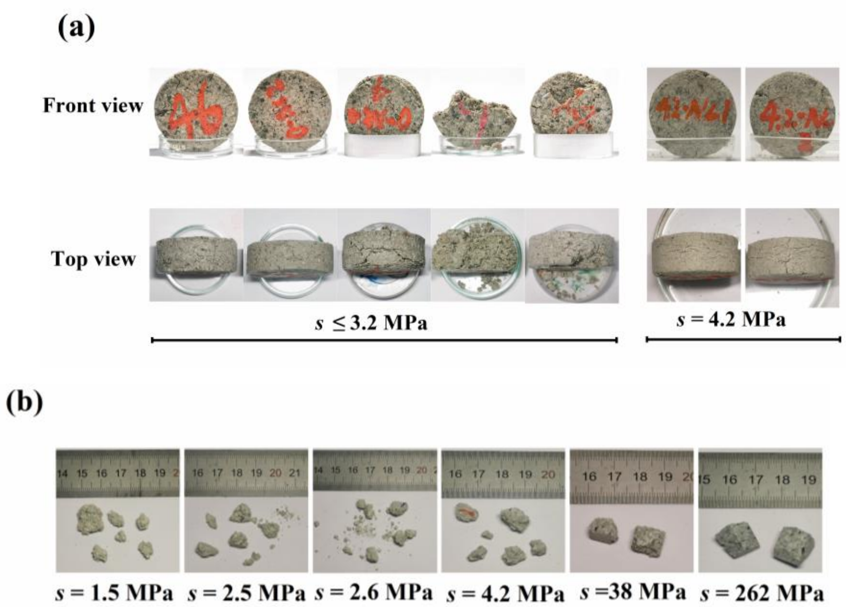

Fig. 11. (a) The fragility of bentonite pellets at $s \leq 4.2$ MPa; (b) The freeze-dried samples at $s \leq 4.2$ MPa, with samples at suctions 38 and 262 MPa selected as reference.

### 4.3 Discussions on µCT results

As far as the grey level threshold on µCT results is concerned, Haugen and Bertoldi [13] pointed out that the thresholding step performed by visual and histogram estimation was user-dependent, possibly resulting in inaccurate structural characterization. In fact, some pixels contained pores (i.e., pores with sizes < 18 µm or the border part with large pores) and bentonite matrix simultaneously, and the contrast of pore and bentonite matrix is the main concern in that case. For instance, the pixels with grey levels around 45 in the zoom-in figure (Fig. 6) may include µCT-non-detection pores and bentonite matrix. The larger the threshold adopted, the more the pores of 18 µm and the larger the pores > 18 µm. Nevertheless, when comparing the thresholds adopted between 25 and 45 for $s$ = 4.2 MPa in Fig. 6, it appears that the large pores that were constituted by dozens of pixels tended to expand insignificantly, while the point-shaped pores that comprised several pixels remarkably increased with the increase of the adopted threshold, indicating that the thresholding has limited effect on the large pores. In other words, the size of large pores identified by µCT is not significantly depending on the thresholding accuracy.

Because the MIP technique appears appropriate for determining the PSD of bentonite pellets at $s \geq 9$ MPa, the thresholding of µCT images was suggested to be adapted to the MIP results, by making µCT-detection $e_{18\text{-}344}$ equal to MIP-detection one at $s \geq 9$ MPa. The thresholds for pellets at $s \geq 57$ MPa were adopted as the previous values in Table 2, while the value 35 was selected as the thresholds at 9 MPa $\leq s \leq$ 25 MPa and the value 40 was selected as the threshold at $s$ = 38 MPa.

The determination of the thresholds for the pellets at $s \leq 4.2$ MPa seems to be less straightforward. Fig. 12(a) shows that the average attenuation coefficients of whole sample, bentonite fabric and µCT-detection pore decreased with the suction decrease from 262 to 4.2 MPa. On the contrary, a slight increase in the average attenuation coefficients of whole sample, bentonite fabric and µCT-detection pore are observed when the suction decreased from 4.2 to 1.5 MPa. It is worth noting that the attenuation coefficients of whole sample and bentonite fabric had exactly the same trend, showing that the bentonite fabric itself dominated the attenuation coefficient of whole sample. The average attenuation coefficient of µCT-detection pores up to 0.006 was due to some pixels containing µCT-non-detection pores and bentonite matrix simultaneously. The water fraction and µCT-non-detection pore fraction in bentonite fabric were determined using Eqs. (3) and (4) respectively and presented in Fig. 12(b).

$$\text{Water fraction} = \frac{V_w}{V_{V,\leq 18} + V_s} = \frac{w G_s}{1 + e_{\mathrm{T}} - e_{\geq 18}} \qquad (3)$$

$$\mu\mathrm{CT}-\mathrm{non}-\mathrm{detection\ pore\ fraction}=\frac{V_{V,\leq 18}}{V_{V,\leq 18}+V_s}=\frac{e_{\mathrm{T}}-e_{\geq 18}}{1+e_{\mathrm{T}}-e_{\geq 18}} \quad (4)$$

where $G_s$ is the specific gravity of bentonite matrix (taken as 2.77), and $V_w$, $V_s$ and $V_{V,\leq 18}$ are the volumes of water, bentonite matrix and pores smaller than 18 μm, respectively. The water content $w$ at suctions 262-1.5 MPa and the total void ratios $e_{\mathrm{T}}$ at suctions 262-4.2 MPa could be taken as the value when reaching suction equilibrium (Fig. 2(b)) and the total void ratios $e_{\mathrm{T}}$ at suctions 3.2, 2.6, 2.5 and 1.5 MPa were measured before the μCT scans, being 1.57, 2.01, 1.73 and 1.86 respectively. The lower the suction the larger the $e_{\mathrm{T}}$, which held for suctions larger than 4.2 MPa. However, upon wetting to suction smaller than 4.2 MPa, the volume change of pellets became unstable - the pellets started to lose their good shape, leading to a relatively large scatter of $e_{\mathrm{T}}$ data at low suctions. It is observed from Fig. 12(b) that the water fraction and μCT-non-detection pore fraction increased with the suction decrease. Jacinto et al. [15] pointed out that the water density for MX80 bentonite sample at a dry density of 1.6 Mg/m$^3$ decreased from around 1.165 Mg/m$^3$ at suction 113 MPa, to 1.13 Mg/m$^3$ at suction 38 MPa, to 1.093 Mg/m$^3$ at suction 4.2 MPa and to 1.085 Mg/m$^3$ at suction 1.5 MPa. Thereby, the decreasing average attenuation coefficient of bentonite fabric at $s \geq 4.2$ MPa was due to the increasing μCT-non-detection pore fraction, the increasing water fraction and the decreasing water density, in agreement with the decrease in attenuation coefficient for the Callovo-Oxfordian claystone upon wetting [26]. However, the increasing average attenuation coefficient of bentonite fabric at $s \leq 3.2$ MPa was hard to be quantified. Considering the difficulty in considering the suction effect on the attenuation coefficient, the MIP results of Molinero-Guerra et al. [19] was taken as reference and the threshold at 1.5 MPa $\leq s \leq$ 3.2 MPa was selected as 40 and the threshold at 4.2 MPa was selected as 35. The corrected μCT-detection $e_{18\text{-}344}$ calculated by the new thresholds matched well with the MIP-detection $e_{18\text{-}344}$, as shown in Fig. 13, completing the μCT-detection in the low suction range. Since there was a limited effect of μCT thresholding on large pores as mentioned previously, the μCT-detection PSD for pore larger than 344 μm was used to extend the upper limit of MIP-detection pore sizes.

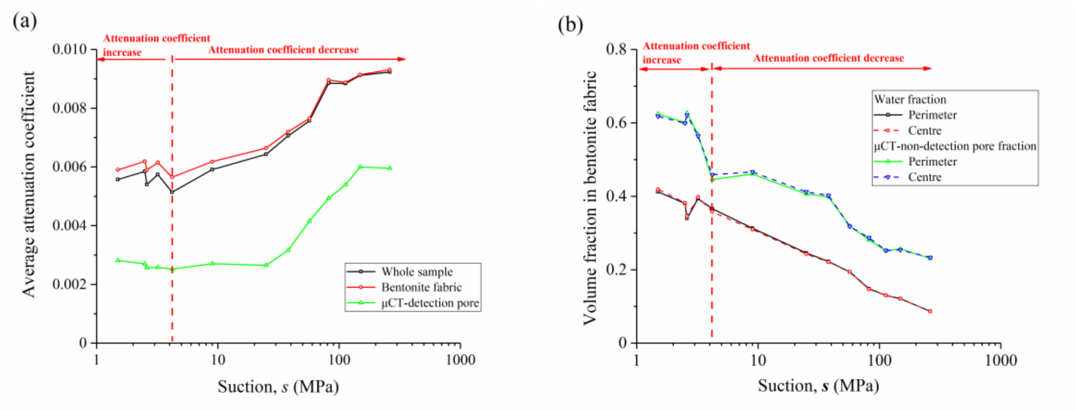

Fig. 12. (a) Average attenuation coefficients of whole sample, bentonite fabric and μCT-detection pore; (b) Volume fractions of water and μCT-non-detection pore in bentonite fabric.

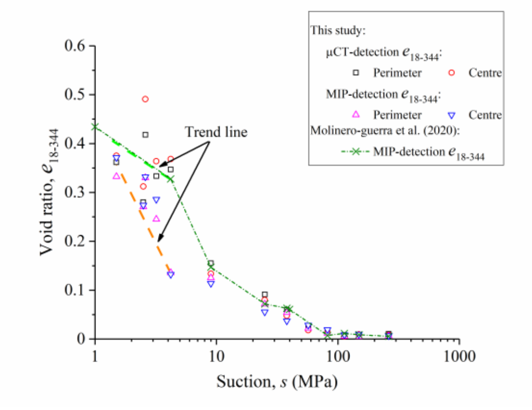

Fig. 13. Corrected $e_{18-344}$ versus suction.

The corrected PSDs by the proposed combined MIP/μCT method for the bentonite pellets at suctions 82, 38, 4.2 and 2.5 MPa are shown in Fig. 14. It appears from Fig. 14(a) that the smaller the suction, the larger the cumulative void ratio. From Fig. 14(b) it is observed that the PSDs displayed a bimodal porosity at $s \geq 4.2$ MPa, but a trimodal porosity at $s = 2.5$ MPa. Moreover, the smaller the suction, the larger the large and small pores. The large pores that the MIP tests cannot identify were not negligible especially at low suctions (Fig. 14(b)), confirming the necessity of combining the MIP and μCT techniques.

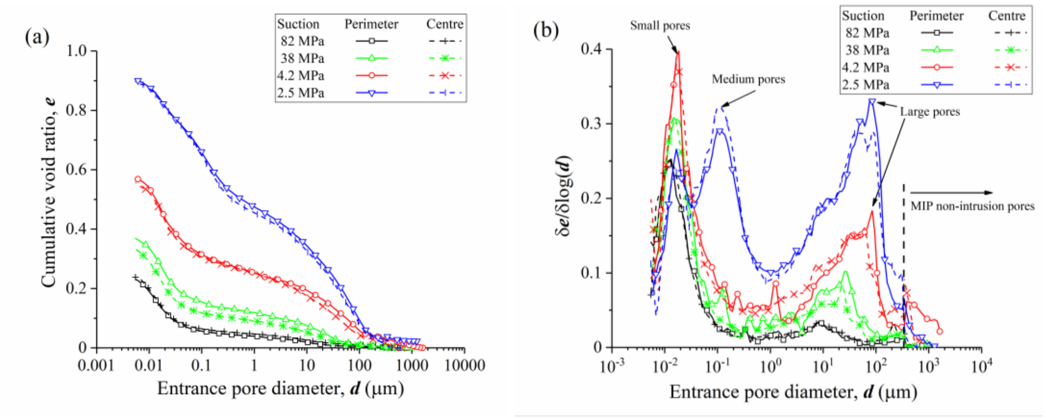

Fig. 14. Corrected pore size distributions of bentonite pellets at suctions 82, 38, 4.2 and 2.5 MPa from a combined MIP/μCT method: (a) cumulative curves; (b) density function curves.

## 5. Conclusions

The porosimetry study on MX80 bentonite pellets under various suctions from 262 to 1.5 MPa was conducted by MIP and μCT techniques. The Stanford segmentation that applies the automatic thresholding together with the manual thresholding was used in image segmentation. The pores with overlapping pore size range (with the void ratio $e_{18\text{-}344}$) for both MIP and μCT were analysed for comparison, allowing a combined MIP and μCT method to be proposed for a large range PSD determination.

The MIP-detection $e_{18\text{-}344}$ nearly overlapped with the μCT-detection one at $s \geq 57$ MPa, indicating the reliability of both MIP and μCT results in this high suction range. However, the μCT-detection $e_{18\text{-}344}$ became larger than the MIP-detection one at 9 MPa $\leq s \leq$ 38 MPa. This is due to the difficulty in the thresholding process while applying the μCT technique. Indeed, such process is user-dependent, which might result in inaccurate structural characterisation. On the contrary, the MIP technique was found to be appropriate at $s \geq 9$ MPa because the problems related to the closed pores and restricted pores appear to be insignificant. Therefore, the segmentation of μCT images was suggested to be corrected based on the MIP results by making the μCT-detection $e_{18\text{-}344}$ equal to the MIP-detection one.

The hydration and exfoliation effects resulted in a significant MIP test data scatter at low suctions

(1.5 MPa ≤ $s$ ≤ 4.2 MPa). The large MIP data scatter was explained by the difficulty in dealing with fragile samples after hydration and freeze-drying, as well as the possibility of underestimating the pore volume because some sampling may be done along large cracks. This could also explain the large difference between the MIP-detection $e_{18\text{-}344}$ of this study and the results of Molinero-Guerra et al. [19] at $s$ ≤ 4.2 MPa. The μCT-detection $e_{18\text{-}344}$ decreased with suction decreasing, as opposed to the MIP-detection $e_{18\text{-}344}$. Considering the difficulty of determining the μCT attenuation coefficient at varying suctions and the reliability of MIP results as mentioned above, it was proposed to use the MIP-detection $e_{18\text{-}344}$ of Molinero-Guerra et al. [19] as a reference for selecting the thresholds at 1.5 MPa ≤ $s$ ≤ 4.2 MPa. For pores larger than 344 μm, as the μCT-detection PSD is appropriate, it could be used to extend the upper limit of MIP-detection pore sizes.

The PSDs of bentonite pellets were thus obtained in a wide range for different suctions, which can be used in further hydro-mechanical analyses.

## Acknowledgments

The authors would like to thank the China Scholarship Council (CSC). The supports provided by Ecole des Ponts ParisTech (ENPC) and Institut de Radioprotection et de Sûreté Nucléaire (IRSN) are also greatly acknowledged.

## Data availability

Data can be available from the authors upon request.

## 6. References

1. Aït-Mokhtar A, Amiri O, Dumargue P, Bouguerra A (2004) On the applicability of Washburn law: Study of mercury and water flow properties in cement-based materials. Mater Struct Constr 37(266):107–113. https://doi.org/10.1617/13857

2. Alonso EE, Romero E, Hoffmann C (2011) Hydromechanical behaviour of compacted granular expansive mixtures: Experimental and constitutive study. Geotechnique 61(4):329–344.

https://doi.org/10.1680/geot.2011.61.4.329

3. Andrä H, Combaret N, Dvorkin J, Glatt E, Han J, Kabel M, Keehm Y, Krzikalla F, Lee M, Madonna C, Marsh M, Mukerji T, Saenger EH, Sain R, Saxena N, Ricker S, Wiegmann A, Zhan X (2013) Digital rock physics benchmarks-Part I: Imaging and segmentation. Comput Geosci 50:25–32. https://doi.org/10.1016/j.cageo.2012.09.005

4. Bevilacqua V, Mastronardi G, Marinelli M (2006) A neural network approach to medical image segmentation and three-dimensional reconstruction. Lect Notes Comput Sci 4113:22–31. https://doi.org/10.1007/11816157_3

5. Cui YJ, Tang AM, Qian LX, Ye WM, Chen B (2011) Thermal-mechanical behavior of compacted GMZ bentonite. Soils Found 51(6):1065–1074. https://doi.org/10.3208/sandf.51.1065

6. Delage P, Marcial D, Cui YJ, Ruiz X (2006) Ageing effects in a compacted bentonite: A microstructure approach. Geotechnique 56(5):291–304. https://doi.org/10.1680/geot.2006.56.5.291

7. Delage P (2007) Microstructure Features in the Behaviour of Engineered Barriers for Nuclear Waste Disposal. Springer Berlin Heidelberg New York, Weimar

8. Diwakar M, Kumar M (2018) A review on CT image noise and its denoising. Biomed Signal Process Control 42:73–88. https://doi.org/10.1016/j.bspc.2018.01.010

9. Fan JL, Lei B (2012) A modified valley-emphasis method for automatic thresholding. Pattern Recognit Lett 33(6):703–708. https://doi.org/10.1016/j.patrec.2011.12.009

10. Van Geet M, Volckaert G, Roels S (2005) The use of microfocus X-ray computed tomography in characterising the hydration of a clay pellet/powder mixture. Appl Clay Sci 29(2):73–87. https://doi.org/10.1016/j.clay.2004.12.007

11. Gens A, Olivella S (2001) Clay barriers in radioactive waste disposal. Rev Française Génie Civ 5(6):845–856. https://doi.org/10.1080/12795119.2001.9692329

12. Hashemi MA, Massart TJ, Salager S, Herrier G, François B (2015) Pore scale characterization of lime-treated sand-bentonite mixtures. Appl Clay Sci 111:50–60. https://doi.org/10.1016/j.clay.2015.04.001

13. Haugen HJ, Bertoldi S (2017) Characterization of morphology-3D and porous structure. Charact Polym Biomater :21–53. https://doi.org/10.1016/B978-0-08-100737-2.00002-9

14. Hoffmann C, Alonso EE, Romero E (2007) Hydro-mechanical behaviour of bentonite pellet mixtures. Phys Chem Earth 32(8–14):832–849. https://doi.org/10.1016/j.pce.2006.04.037

15. Jacinto AC, Villar M V., Ledesma A (2012) Influence of water density on the water-retention curve of expansive clays. Geotechnique 62(8):657–667. https://doi.org/10.1680/geot.7.00127

16. Karmazyn B, Liang Y, Klahr P, Jennings SG (2013) Effect of tube voltage on ct noise levels in different phantom sizes. Am J Roentgenol 200(5):1001–1005. https://doi.org/10.2214/AJR.12.9828

17. Li P, Shao S (2020) Can X-ray computed tomography (CT) be used to determine the pore-size distribution of intact loess? Environ Earth Sci 79(1):1–12. https://doi.org/10.1007/s12665-019-8777-z

18. Mokni N, Molinero-Guerra A, Cui YJ, Delage P, Aimedieu P, Bornert M, Tang AM (2020) Modelling the long-term hydro-mechanical behaviour of a bentonite pellet/powder mixture with consideration of initial structural heterogeneities. Geotechnique 70(7):563–580

19. Molinero-Guerra A, Delage P, Cui YJ, Mokni N, Tang AM, Aimedieu P, Bernier F, Bornert M (2020) Water-retention properties and microstructure changes of a bentonite pellet upon wetting/drying; application to radioactive waste disposal. Geotechnique 70(3):199–209. https://doi.org/10.1680/jgeot.17.P.291

20. Molinero-Guerra A, Mokni N, Delage P, Cui YJ, Tang AM, Aimedieu P, Bernier F, Bornert M (2017) In-depth characterisation of a mixture composed of powder/pellets MX80 bentonite. Appl Clay Sci 135:538–546. https://doi.org/10.1016/j.clay.2016.10.030

21. Ng HP, Ong SH, Foong KWC, Goh PS, Nowinski WL (2006) Medical image segmentation using k-means clustering and improved watershed algorithm. Proc IEEE Southwest Symp Image Anal Interpret 2006(April 2014):61–65. https://doi.org/10.1109/ssiai.2006.1633722

22. Otsu N, Smith PL, Reid DB, Environment C, Palo L, Alto P, Smith PL (1979) A Tlreshold Selection Method from Gray-Level Histograms. IEEE Trans Syst Man Cybern C(1):62–66

23. Romero E, Simms PH (2008) Microstructure investigation in unsaturated soils: A review with special attention to contribution of mercury intrusion porosimetry and environmental scanning electron microscopy. Geotech Geol Eng 26(6):705–727. https://doi.org/10.1007/s10706-008-9204-5

24. Saiyouri N, Tessier D, Hicher P (2004) Experimental study of swelling in unsaturated compacted clays. Clay Miner 39(4):469–479

25. Saxena N, Hofmann R, Alpak FO, Dietderich J, Hunter S, Day-Stirrat RJ (2017) Effect of image segmentation & voxel size on micro-CT computed effective transport & elastic properties. Mar Pet Geol 86:972–990. https://doi.org/10.1016/j.marpetgeo.2017.07.004

26. Stavropoulou E, Andò E, Roubin E, Lenoir N, Tengattini A, Briffaut M, Bésuelle P (2020) Dynamics of Water Absorption in Callovo-Oxfordian Claystone Revealed With Multimodal X-Ray and Neutron Tomography. Front Earth Sci 8(March). https://doi.org/10.3389/feart.2020.00006

27. Sun H, Mašín D, Najser J, Nedela V, Navrátilová E (2019) Bentonite microstructure and saturation evolution in wetting-drying cycles evaluated using ESEM, MIP and WRC measurements. Geotechnique 69(8):713–726. https://doi.org/10.1680/jgeot.17.P.253

28. Tang AM, Cui YJ (2005) Controlling suction by the vapour equilibrium technique at different temperatures and its application in determining the water retention properties of MX80 clay. Can Geotech J 42(1):287–296. https://doi.org/10.1139/t04-082

29. Tugwell-Allsup JR, Morris RWYN, Thomas K, Hibbs R, England A (2022) Neonatal digital chest radiography– should we be using additional copper filtration? Br J Radiol 95(1130).

https://doi.org/10.1259/bjr.20211026

30. Wang H (2021) Delayed and Swelling Behaviour of Damaged/Fractured Callovo-Oxfordian Claystone. (Doctoral dissertation, Ecole des Ponts Paristech)

31. Wang Q, Cui YJ, Tang AM, Barnichon JD, Saba S, Ye WM (2013) Hydraulic conductivity and microstructure changes of compacted bentonite/sand mixture during hydration. Eng Geol 164:67–76. https://doi.org/10.1016/j.enggeo.2013.06.013

32. Washburn EW (1921) The dynamics of capillary flow. Phys Rev 17(3):273–283. https://doi.org/10.1103/PhysRev.18.206

33. Ying Z, Cui YJ, Benahmed N, Duc M (2023) Drying effect on the microstructure of compacted salted silt. Geotechnique 73(1):62–70. https://doi.org/10.1680/jgeot.20.P.319

34. Yuan S, Liu X, Wang Y, Delage P, Aimedieu P, Buzzi O (2022) Applied Clay Science X-Ray microtomography of mercury intruded compacted clay : An insight into the geometry of macropores. 227(June)

35. Zeng Q, Chen S, Yang P, Peng Y, Wang J, Zhou C, Wang Z, Yan D (2020) Reassessment of mercury intrusion porosimetry for characterizing the pore structure of cement-based porous materials by monitoring the mercury entrapments with X-ray computed tomography. Cem Concr Compos 113:1–16. https://doi.org/10.1016/j.cemconcomp.2020.103726

36. Zeng Q, Wang X, Yang P, Wang J, Zhou C (2019) Tracing mercury entrapment in porous cement paste after mercury intrusion test by X-ray computed tomography and implications for pore structure characterization. Mater Charact 151:203–215. https://doi.org/10.1016/j.matchar.2019.02.014

37. Zeng Z (2021) Investigation of the hydro-mechanical behaviour of compacted bentonite/claystone mixture. (Doctoral dissertation, Ecole des Ponts Paristech)

38. Zeng Z, Cui YJ, Talandier J (2022) Evaluation of swelling pressure of bentonite/claystone mixtures from pore size distribution. Acta Geotech 5:1–9. https://doi.org/10.1007/s11440-022-

01676-5

39. Zong Y, Yu X, Zhu M, Lu S (2015) Characterizing soil pore structure using nitrogen adsorption, mercury intrusion porosimetry, and synchrotron-radiation-based X-ray computed microtomography techniques. J Soils Sediments 15(2):302–312. https://doi.org/10.1007/s11368-014-0995-0